



### **Science Arts & Métiers (SAM)**

is an open access repository that collects the work of Arts et Métiers Institute of Technology researchers and makes it freely available over the web where possible.

This is an author-deposited version published in: <https://sam.ensam.eu>  
Handle ID: [.http://hdl.handle.net/10985/17358](http://hdl.handle.net/10985/17358)

#### **To cite this version :**

Ba Danh LE, Jean-Luc CHARLES, Ivan IORDANOFF, Frédéric DAU - Modeling damages and cracks growth in composite with a 3D discrete element method - Composites Part B: Engineering - Vol. 91, p.615-630 - 2016

Any correspondence concerning this service should be sent to the repository

Administrator : [scienceouverte@ensam.eu](mailto:scienceouverte@ensam.eu)



# Modeling damages and cracks growth in composite with a 3D discrete element method

B.D. Le, F. Dau<sup>\*</sup>, J.L. Charles, I. Iordanoff

*Department of Durability of Materials, Assemblies and Structures (DuMAS), Arts et Metiers ParisTech, I2M, UMR 5295 CNRS F-33400, Talence, France*

## A B S T R A C T

This paper presents a 3D simulation of damages and cracks growth in composite material using Discrete Element Method (DEM). Fiber/matrix debonding and ply to ply delamination, cracks matrix, rupture of fibers are addressed. Matrix and fiber are supposed to be brittle materials and follow a linear fracture model. Cohesive contact laws are implemented to model interfaces behavior for both debonding (fiber/matrix) and delamination (ply/ply). Piecewise linear elastic laws usually used in cohesive zone models are retained in this work. A Double Cantiliver Beam (DCB) test is first experimented using the present DEM with Cohesive Contact Models (CCM). Then, based on De Borst's works [1], a single fiber composite under transverse traction is modeled to study debonding and matrix cracks propagations depending on the matrix and the fiber/matrix interface strengths ratio. A bi-disperse medium for matrix and fiber is specifically elaborated to reduce the discrete elements number. The analysis is extended to a so-called multi-fibers composite specimen, also called Statistical Elementary Volume (SEV), made of several fibers embedded in the matrix. Finally, the results are compared with DeBorst's works and qualitatively discussed.

## Keywords:

A. Polymer-matrix composite  
C. Numerical analysis  
C. Damage mechanics  
Discrete element method

## 1. Introduction

Taking benefits of their specific properties, composite materials are widely used for structural applications in various industry but particularly in the aerospace industry. Composite structure always need to be more and more optimized for economic and environmental reasons in particular. So, many efforts are made today in manufacturing but also and simultaneously in modeling. Indeed, the damage mechanisms and their growth when composite materials and structures are exposed to severe loading must be predicted as precisely as possible. Delamination Fig. 1 and fiber/matrix debonding Fig. 2 are mainly addressed. In this purpose, modelizations must take place at microscopic scales to capture such damages.

Currently, numerical methods are based on the continuum damage mechanics and the fracture mechanics for both studying the damage initiation and the cracks propagation. They use a stress criteria for initiation [4,5] and a strain energy release rate for propagation [6–9]. The Virtual Crack Closure Technique (VCCT) is also encountered to predict only the propagation of existing

delaminations [10–12]. Another way is to use cohesive zone model [13–15]. Compared with the VCCT, it offers the advantages of the crack initiation, the crack propagation with no need of time consuming crack-paths algorithms. Multiple crack paths can be considered but needs to place cohesive interface elements everywhere the crack may propagate [16]. In this case, the numerical treatment can rapidly increase and happens to be very time consuming. Moreover, modeling fiber/matrix debonding this way is not possible.

To overcome these difficulties, the use of a 3D Discrete Element Method (DEM) is a very interesting alternative. In Refs. [17], authors have demonstrated the ability of the method to naturally capture the damages and their growth in composite medium without preset paths. The present paper is a continuity of this work. The main improvements remain in the implementation of a Cohesive Contact Model (CCM) to model fiber/matrix debonding and delamination, but also in the introduction of a bi-disperse medium to save significant computation time; the size of Discrete Elements (DE) is larger for the fiber than for the matrix. Besides, the added value of the present DEM is to be in 3D whereas the most of DEM investigated for composite medium in literature are in 2D [18–22].

In this paper, the general concept of the present DEM developed in the lab is first recalled. Then, the geometrical modelization of the composite medium as a bi-disperse medium is presented; a single

<sup>\*</sup> Corresponding author. Tel.: +33 556845335.  
E-mail address: f.dau@i2m.u-bordeaux1.fr (F. Dau).

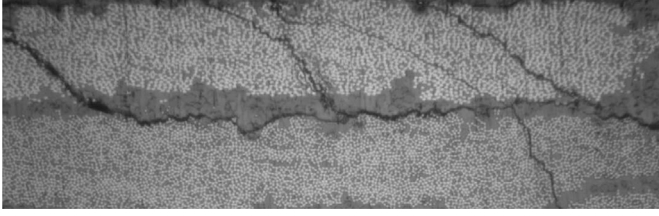


**Fig. 1.** Delamination at the interface between two plies of carbon fiber reinforced polymer composite under an impact laser [2].

fiber composite and statistical elementary volumes are considered. Next, the mechanical modelization for fiber, matrix and fiber/matrix interface using the Cohesive Contact Model (CCM) is described. The following sections are devoted to numerical tests. A Double Cantilever Beam (DCB) test is first experimented using the present DEM with cohesive contact models. Then, based on De Borst's works [1], a single fiber composite under transverse traction is modeled to study debonding and matrix cracks propagations depending on the matrix and the fiber/matrix interface strengths ratio. This test is extended to the so-called Statistical Elementary Volume (SEV) made of several fibers embedded in the matrix. Finally, the results are compared with DeBorst's works and qualitatively discussed.

## 2. Discrete element modeling

### 2.1. Granular Object Oriented workbench

The DEM originally developed by Cundall and Strack [23] is a very useful numerical tool for modeling the behavior of granular and particulate material [24–27]. Further developments have adapted the method to study the fracture of brittle materials such as concrete and rocks [28–30], composite [18,19]. In DEM, the materials are discretized by a great number of DE interacting with each other. The DE are of spherical (3D) [23,31], or circular (2D) [32,33], or polyhedral shapes [34,35]. They interact by contact, spring and dampers links [36,21,22] or by cohesive beams [31,37,38]. The contact laws can be regular [23,34,35] or non regular ones [39]. The constitutive parameters of spring, dampers links and cohesive beams are calibrated to get the suitable behavior at an observable scale. Then elasticity, plasticity, viscosity and more complex behavior can be addressed. A brittle elastic behavior is considered in the present work.

In this study, the *Granular Object Oriented workbench (GranOO)* software developed in the lab [40] is used. In *GranOO*, calculations are based on Verlet velocities [41] explicit dynamics integration

scheme. The discrete element linear position and velocity are estimated by Ref. [42]:

$$\vec{p}(t + dt) = \vec{p}(t) + dt \vec{v}(t) + \frac{dt^2}{2} \vec{a}(t) \quad (1)$$

$$\vec{v}(t + dt) = \vec{v}(t) + \beta \frac{dt}{2} (\vec{a}(t) + \vec{a}(t + dt)) \quad (2)$$

where:

- $t$  is the current time and  $dt$  is the integration time step.
- $\vec{p}(t)$ ,  $\vec{v}(t)$ ,  $\vec{a}(t)$  is the discrete element linear position, velocity and acceleration.
- $\beta$  is the numerical damping factor.

Compared to others explicit schemes [43], Verlet scheme has been selected thanks to its ability to provide goods results and its ease of implementation. Knowing the DE position and velocity, the interacting forces and couples are calculated. Then, the dynamical equilibrium applied on each DE leads to the DE acceleration. The new velocity and position are then obtained by integrations and so on. A flow chart of Verlet dynamics explicit scheme for linear position and velocity is illustrated in Table 1. The same scheme for angular position and velocity.

The time step is proportional to the square root of the ratio between the smallest mass and the greater stiffness. Its final value is chosen to get a stable integration numerical scheme. Moreover, an artificial damping can be advantageously introduced to prevent from large numerical oscillations due to high frequencies.

DE used in *GranOO* are mainly of spherical shape but there is no restrictions to use more complex shapes if needed by the study. For instance, for thermal conduction, polyhedral particules can be used. The radius of spheres is varying according to a uniform distribution to optimize the filling process of the continuum medium avoiding a special arrangement of DE, see Section 2.2. Otherwise, regular contact laws and cohesive beams are used in *GranOO* in 3D model [42]. Fig. 3 illustrates the cohesive bonding of the beam type of a discrete domain. The beam is cylindrical. Its geometry is defined by only two parameters: the length  $L_\mu$  and the radius  $r_\mu$  where the subscript  $\mu$  stands for microscopic scale. Details on the geometrical and mechanical aspects are given in the next sections.

### 2.2. Geometrical modeling - mono and bi-disperse media

#### 2.2.1. Specimens type

Two types of specimen are considered in this work related to the performed study.

For delamination study, the Double Cantilever Beam (DCB) test in 3D is performed. The specimen is made of two plies (Fig. 4)(a). It

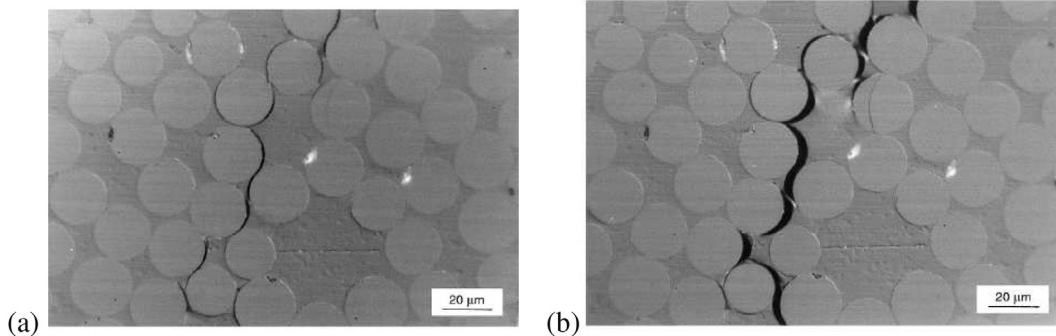


**Fig. 2.** Fiber-matrix debonding: section perpendicular to the fiber axis [3].

**Table 1**  
Verlet dynamics explicit scheme.

---

**Require:**  $\vec{p}(0), \vec{p}(0), \vec{p}(0)$   
 $t \leftarrow 0$   
**for all** iteration  $n$  **do**  
  **for all** discrete element  $i$  **do**  
     $\vec{p}_i(t + dt) \leftarrow$  Linear position Verlet scheme (Eq.1)  
     $\vec{f}_i(t + dt) \leftarrow$  Sum of force acting on  $i$   
     $\vec{p}_i(t + dt) \leftarrow$  Newton second law  
     $\vec{p}_i(t + dt) \leftarrow$  Linear velocity Verlet scheme (Eq.2)  
  **end for**  
   $t \leftarrow t + dt$   
**end for**

---

constitutes a so-called mono-disperse medium supposed to be isotropic.

For debonding and matrix cracks study, the traverse traction test on mono-fiber and multi-fibers embedded in a resin block proposed by Alfaro et al. [1] is investigated. A bi-disperse medium is then elaborated for the composite. The DE for modeling fibers are greater than the ones for matrix. Indeed, for fibers, the DE radius is equal to the radius of the fiber supposed to be of circular cylindrical shape. The DE are then stacked along the fiber with geometrical overlapping to properly represent the fiber/matrix interface. Finally, it looks like a pearl necklace where the pearls geometrically interpenetrate with each other. This modeling is convenient since the intra-fiber damages are not sought. For matrix, the DE are smaller. Their size is chosen so that cracks initiation and propagations could be captured. The single fiber and the composite specimens with mono and multi-fibers are depicted in Fig. 4(b), (c) and (d). By adopting such a bi-disperse medium for mono-fiber and multi-fibers composite specimens, the number of DE and so the computational time can be significantly decreased.

### 2.2.2. Filling process

The filling process is the way to build a compacted discrete domain that represents a continuous homogeneous isotropic domain. It is challenged by the following objectives [42]: i) to reach a rate of compaction for modeling correctly the continuums, ii) to insure the medium isotropy (at this stage, fiber and matrix are supposed to be isotropic), iii) to preserve the interface geometry (ply/ply and fiber/matrix) as precise as possible.

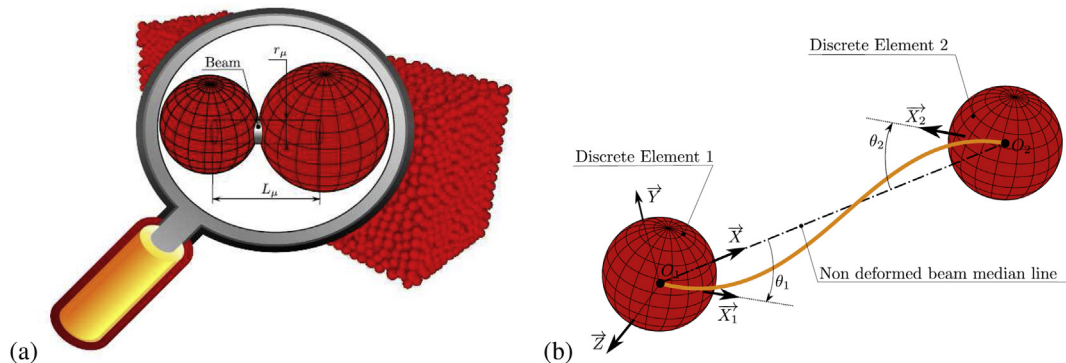


**Fig. 3.** Illustration of the cohesive beam bond in GranOO [42].

The common filling procedure is performed in three distinct steps: i) a random free filling, ii) a forced filling, iii) a relaxation phase of the domain [42].

- In the first step, the volume to be filled is defined. DE are randomly placed in this volume. Each DE has a random radius following a given statistical distribution (uniform, truncated Gaussian). The radius dispersion is about 25%. The volume bounding surfaces behave as rigid walls. This first step of filling ends when no more DE can be randomly added without geometrical inter-penetration with each other.
- The second step consists in completing the filling by forcing the inter-penetration between the DE. When no more DE can be placed without exceeding the inter-penetration tolerance, a DEM calculation is performed to allow a re-arrangement of the discrete domain. Then, new DE can be placed. This operation is repeated till the minimal coordination number obtained of 6.2 is achieved.
- The last step is a relaxation of the discrete domain to reduce the inter-penetrations between DE. The method used consists in lowering gradually the stiffness of the bounding rigid walls. The relaxation stops when an acceptable inter-penetration value (smaller than  $10^{-5}\%$ ) is achieved.

The specimen used for DCB test (Fig. 4)(a) has been created by applying the three steps above. For the composite specimens, Fig. 4(c) and (d), the bi-disperse medium required a special pre-filling step. It consists in placing the fiber DE before performing the common filling procedure. Thus, the fiber DE are randomly placed in the cubic matrix volume to be filled. The number of fibers depends on the desired fiber volume fraction. The fiber DE don't move during the filling process. Fig. 5 and Fig. 6 illustrate the three steps filling procedure for mono-fiber and multi-fibers composite media with respective fiber volume fraction of  $V_f=0.1$  and  $V_f=0.4$ .

### 2.3. Mechanical modeling: cohesive beams, springs, cohesive contact at interface and matrix failure criteria

Once the geometry of specimens is achieved, the mechanical behavior is considered. For the mono-disperse medium, Fig. 7(a), cohesive beams are placed between the DE of each ply. At interface, the cohesive beams are removed. They are replaced by cohesive contact laws detailed in sections below. For the bi-disperse medium, Fig. 7(b), spring links are introduced to connect the DE of a fiber while cohesive beams are used between the DE of the matrix. Spring stiffness can be obtained analytically from the fiber mechanical properties.

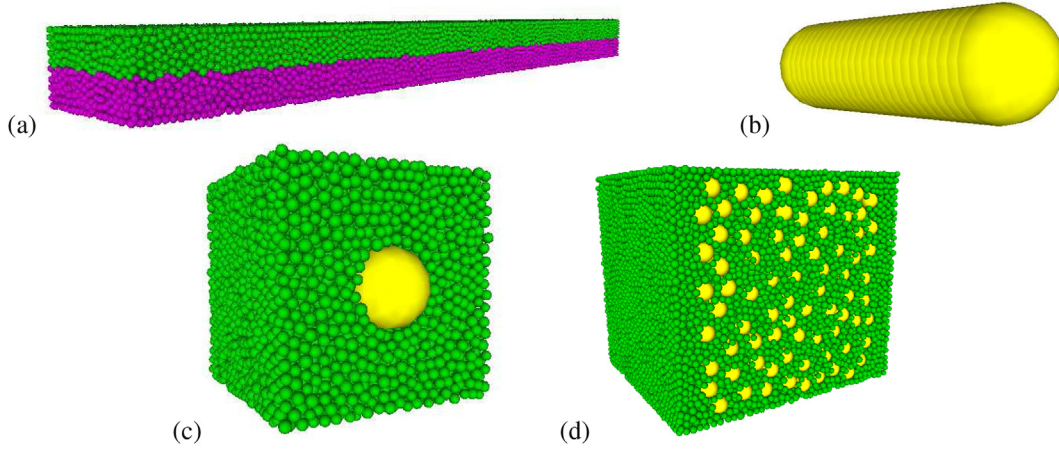


Fig. 4. Sample configuration of a) DCB test (40000 DE), b) single fiber (25 DE), c) mono-fiber composite (10000 DE), d) multi-fibers composite (34000 DE).

### 2.3.1. Interface decohesion - cohesive contact models (CCM)

Cohesive contact laws taking place between the DE in contact at interface (ply/ply, fiber/matrix) are implemented, Fig. 8. Piece-wise linear laws are retained for modeling both normal and shear contact. This contact softening model is quite similar to the cohesive contact model (CCM) used in the continuum mechanics [44,45]. The normal and shear cohesive forces are respectively expressed as a function of the normal displacement  $u_n$  and the tangential displacement  $u_s$  between two particles in contact at interface. Let us define by  $\vec{n}$  the normal vector pointing from the center  $O_1$  of DE 1 to the center  $O_2$  of DE 2, Eq. (3), and by  $\vec{t}$  the tangential vector, orthogonal to  $\vec{n}$ . The normal and tangential displacements can be easily calculated, Eq. (4).  $R_1$  and  $R_2$  respectively denote the radius of DE 1 and DE 2,  $V_t$  is the relative tangential velocity between two particles,  $dt$  is the time step and  $N$  is iteration number.

$$\vec{n} = \overrightarrow{O_1O_2} / \|\overrightarrow{O_1O_2}\| \quad (3)$$

$$u_n = O_1O_2 - (R_1 + R_2) \quad u_s = \sum_{i=1}^N V_t dt \quad (4)$$

For both tensile and shear cases, the interface begins to degrade when the displacements  $u_n$  and  $u_s$  reach respectively the values  $u_n^e$  and  $u_s^e$  corresponding to the critical forces  $F_n^c$  and  $F_s^c$ . The degradation of the interface continues until the displacements reach the values  $u_i^p$ ,  $i = n$  or  $s$ . Then, the crack opens at interface and can propagate in mode I (crack opening), mode II or mode III (shear) and mixte-mode [19].

The fracture energy release rate  $G$  can be easily expressed for both mode I and mode II by Eq. (5):

$$G_I = \frac{1}{2} \frac{F_n^c}{S} u_n^p \quad G_{II} = \frac{1}{2} \frac{F_s^c}{S} u_s^p \quad (5)$$

In the above expressions,  $S$  denotes a fictitious surface between two DE at interface. This surface is simply expressed as  $S = \pi R^2$  where  $R$  stands for an equivalent radius depending on the nature of the medium:

- For the mono-disperse medium,  $R = 0.5(R_1 + R_2)$  with  $R_1, R_2$  the radius of the particles in contact at interface (Fig. 9a).
- For the bi-disperse medium,  $R \approx R_1$  assuming that the value  $R_2 \gg R_1$  with  $R_1$ , the radius of DE of matrix and  $R_2$ , the radius of DE of fiber (Fig. 7)(b).

### 2.3.2. Failure criteria for the matrix

The matrix is modeled as an homogeneous and isotropic brittle material. The DE that constitute the matrix are connected by cohesive beams (see Fig. 7(b)). Two failure criteria for the brittle matrix have been compared in this study. The present criteria have been already investigated in recent works of authors [17]. The first one is based on the literature [34,46], whereas the second one has been developed in the lab [47,48].

The first criterion, called the Breakable Bonds Failure process, *BBF*, is driven by the maximum normal stress in a beam. It simply stipulates that the failure occurs when this maximum normal stress,  $\sigma_{fail}$  is exceeded. Fig. 10 presents an illustration of this failure criterion. Then, a crack can propagate following the path given by the successive breaks of the beams (or bonds).

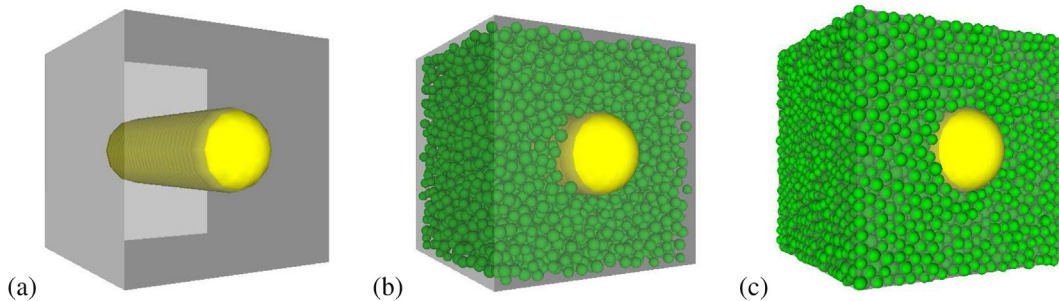
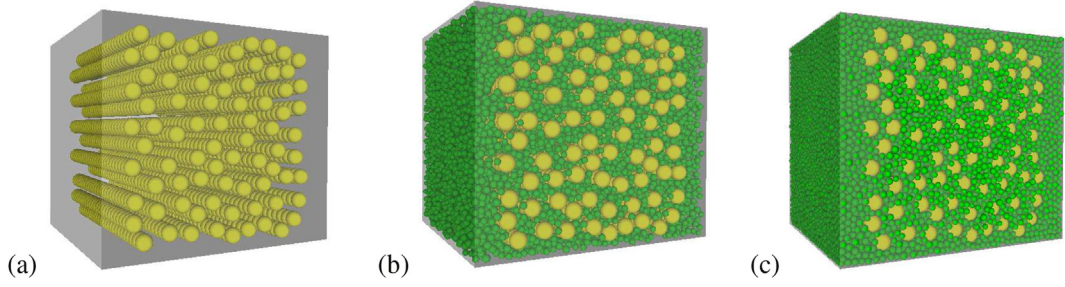
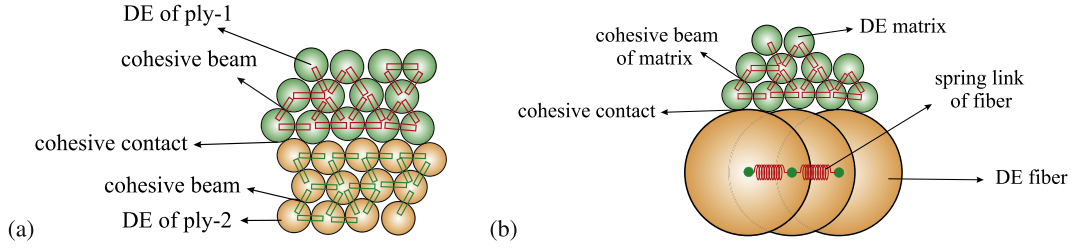


Fig. 5. Filling procedure for mono-fiber composite,  $V_f = 0.1$  (a) pre-filling stage, (b) intermediate stage and (c) final compacted domain.



**Fig. 6.** Filling procedure for multi-fibers composite,  $V_f = 0.4$  (a) pre-filling stage, (b) intermediate stage and (c) final compacted domain.



**Fig. 7.** Mechanical bonds and cohesive laws for (a) mono-disperse and (b) bi-disperse media.

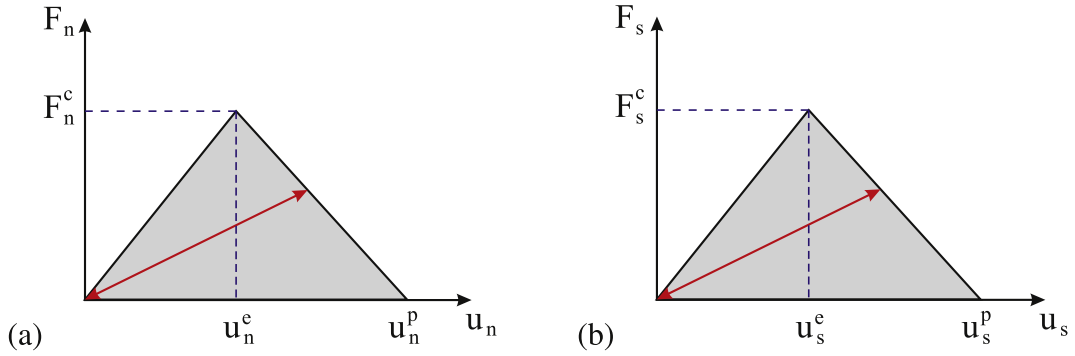


**Fig. 8.** Constitutive behavior of contact softening model (a) normal contact (b) shear contact.

The second criterion, called the Removed DE Failure process, *RDEF*, is based on the deletion of a DE when a tensile criterion is satisfied in bonds connected to this DE. The virial tensor is defined for each DE, as follows:

$$\vec{\sigma}_i = \frac{1}{2\Omega_i} \sum_{j \neq i} \frac{1}{2} \left( \vec{r}_{ij} \otimes \vec{f}_{ij} + \vec{f}_{ij} \otimes \vec{r}_{ij} \right) \quad (6)$$

where:

- $\otimes$  is the tensor product
- $\vec{\sigma}_i$  is the equivalent Cauchy stress tensor for the discrete element  $i$
- $\Omega_i$  is an influential volume around the discrete element  $i$
- $\vec{f}_{ij}$  is the force exerted on the discrete element  $i$  by a cohesive beam that bonds the discrete element  $i$  to another discrete element  $j$
- $\vec{r}_{ij}$  is the relative position vector between the center of the two bonded discrete elements  $i$  and  $j$

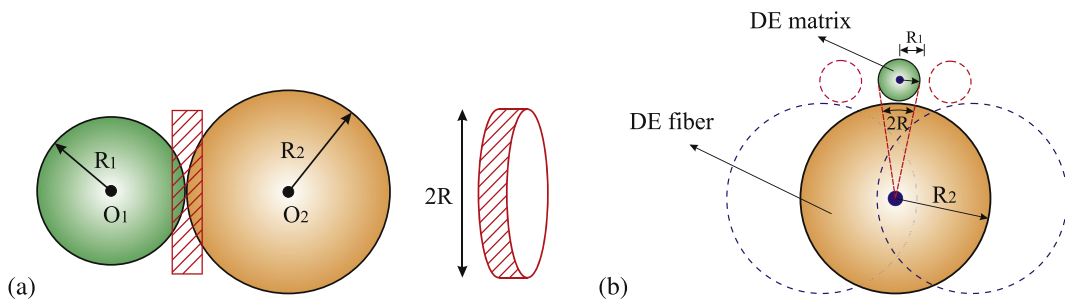


**Fig. 9.** Cohesive contact in (a) mono-disperse (b) bi-disperse media.

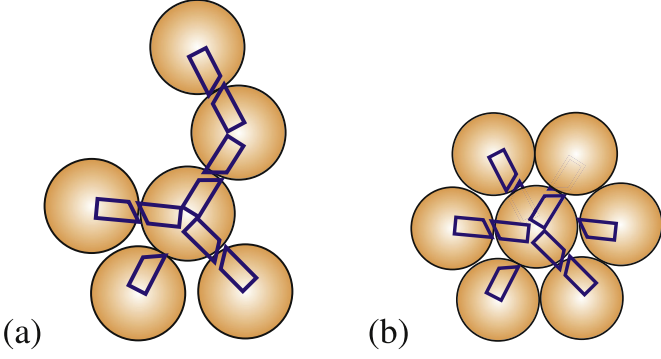


Fig. 10. Illustration of breaking bond for (a) BBF criterion and (b) RDEF criterion.

This criterion assumes that fracture occurs when the hydrostatic stress is higher than a threshold critical value  $\sigma_c$  [48]:

$$\frac{1}{3} \text{trace}(\bar{\sigma}_i^T) \geq \sigma_{fail} \quad (7)$$

When the criterion is satisfied, all the cohesive beams in  $\Omega_i$  around the discrete element  $i$  are broken Fig. 10(b).

The microscopic values of  $\sigma_{fail}$  in BBF criterion and RDEF criterion are obtained by a numerical calibration procedure [48].

### 3. Simulation of DCB test

The implemented cohesive contact models (CCM) are firstly experienced for the Double Cantilever Beam (DCB) test. The subsections below describe the test configuration, the DEM modeling and give a comparison of the numerical results with the analytical solution.

#### 3.1. Test configuration

The geometry of the cantilever beam is shown in Fig. 11. The length, the width and the thickness of the beam are respectively  $L = 45 \text{ mm}$ ,  $b = 6 \text{ mm}$  and  $2h = 3 \text{ mm}$ . A pre-crack of length  $a_0 = 0.3 L$  is performed.  $P$  forces are applied on each part of the pre-cracked beam in order to initiate and propagate a crack, in modes I, from the left to the right end of the specimen. The mechanical properties chosen for quantitative assessment are:  $E = 135 \text{ GPa}$  for Young's modulus,  $\nu_{22} = 0.24$  for Poisson's ratio.  $\sigma_{max} = 5.7 \text{ MPa}$  for the interface strength and  $G_I = 0.56 \text{ N/mm}$ . For this test, only the normal cohesive contact law has been implemented.

#### 3.2. Analytical results

From elastic beam theory, the compliance of the specimen is defined by Eq. (8):

$$C = \frac{2\Delta}{P} = \frac{2a^3}{3EI} \quad (8)$$

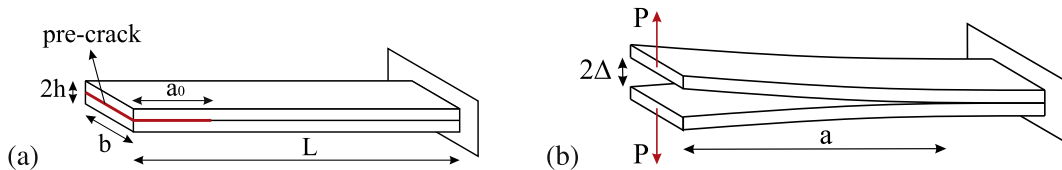


Fig. 11. Illustration of DCB test in continuous medium at (a) initial state (b) loaded state.

where  $a$  is the crack length,  $EI$  is the flexural rigidity of the specimen and  $\Delta$  is the displacement (Fig. 11(b)). Based on energy considerations and remaining in the linear fracture mechanics assumptions, the variation of the compliance can be related to the crack length one using the energy release rate by Eq. (9):

$$G = \frac{P^2}{2b} \frac{dC}{da} = \frac{P^2 a^2}{bEI} \quad (9)$$

where  $b$  is the specimen width.

From Eq. (8) and Eq. (9), and providing that the interface fracture energy is constant during the crack propagation, the force  $P$  versus displacement  $\Delta$  can be expressed as, Eq. (10):

$$P = \sqrt{\frac{4}{9} b^3 G^3 EI} \frac{1}{\sqrt{2\Delta}} \quad (10)$$

The crack length during the crack propagation can be also deduced, Eq. (11):

$$a = \sqrt[4]{\frac{3}{4} \frac{Eh^3 \Delta^2}{G}} \quad (11)$$

### 3.3. DEM modeling

#### 3.3.1. Specimen creation

The DCB specimen building process has been presented in Section 2.2. Firstly, a parallelepiped box of dimensions  $45 \text{ mm} \times 6 \text{ mm} \times 3 \text{ mm}$  was filled by DE. Two specimens with respectively 40000 DE and 60000 DE have been realized. All the DE are connected by the cohesive beam bonds. Then, beam bonds which belong to the interface surface located at mid-thickness of the specimen are removed. They are replaced by cohesive contact laws, detailed in Section 2.3.1, implemented between DE that are in contact at this interface except in the pre-cracked area, Fig. 12.

#### 3.3.2. Calibration of microscopic parameters

This procedure is used to identify the microscopic parameters of the cohesive beam bonds. The cohesive beams are defined by four parameters: two geometrical parameters, the length  $L_\mu$  and the radius  $r_\mu$ , and two mechanical ones in case of linear behavior, the Young's modulus  $E_\mu$  and the Poisson's ratio  $\nu_\mu$ . Practically, an adimensional radius  $\tilde{r}_\mu$  which does not depend on the DE sizes is preferred to  $r_\mu$  for all cohesive beams. It is defined by the ratio between the cohesive beam radius and the average discrete element radius:  $\tilde{r}_\mu = r_\mu / R_{DE}$ . As previously introduced in Section 2.1, the subscript  $\mu$  denotes here and thereafter the microscopic scale.

This calibration procedure is largely described in Ref. [42]. Only the main important points are recalled in this section through the present applications.

The values of the cohesive beam length  $L_\mu$  depends on the distance between the centers of DE interacting. They result from the filling process. The three others parameters  $E_\mu$ ,  $\nu_\mu$ ,  $\tilde{r}_\mu$  need to be

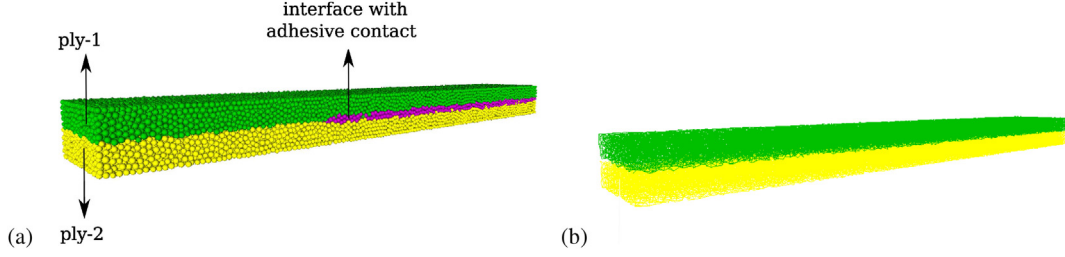


Fig. 12. Configuration of DCB test in DEM model (40000 DE): (a) DE (b) cohesive beam bonds level.

calibrated. The calibration methodology aims to find the suitable microscopic parameters to recover the properties observable at a scale above. It is based on numerical static and dynamic reference tests in traction/compression, bending and torsion.

André et al. [42] have observed that: i) the microscopic Poisson's ratio  $\nu_\mu$  does not influence on the macroscopic Young's modulus  $E_M$  and the macroscopic Poisson's ratio  $\nu_M$  ii) the macroscopic Poisson's ratio  $\nu_M$  depends only on the microscopic radius ratio  $\tilde{r}_\mu$  iii) the macroscopic Young's modulus  $E_M$  depends on the microscopic radius ratio  $\tilde{r}_\mu$  and the microscopic Young's modulus  $E_\mu$ .

With these observations, the calibration methodology can be summarized in two main steps:

- i) and ii) lead to choose initial values for  $\nu_\mu$  and  $E_\mu$ . The respective value of 0.3 and 1000 GPa are arbitrarily adopted. Then,  $\tilde{r}_\mu$  varies and the calibration curve of  $\nu_M$  versus  $\tilde{r}_\mu$  is numerically established, Fig. 13(a). The microscopic value of  $\tilde{r}_\mu$  corresponding to the desired macroscopic value  $\nu_M$  can be extracted from the previous curve. For the present material, the suitable microscopic radius ratio  $\tilde{r}_\mu = 0.49$  is found to match with the desired macroscopic Poisson's ratio value  $\nu_M = 0.24$ .
- knowing the value of  $\tilde{r}_\mu = 0.49$ , the microscopic Young's modulus  $E_\mu$  varies in turn. The calibration curve of the macroscopic Young's modulus  $E_M$  versus the microscopic Young's modulus  $E_\mu$  can be plotted, Fig. 13(b). The microscopic Young's modulus  $E_\mu = 1100$  GPa leading to the desired macroscopic Young's modulus  $E_M = 135$  GPa can thus be obtained.

Concerning the microscopic parameters of the cohesive contact models ( $u_n^e$ ,  $u_n^p$ ,  $F_n^c$ ), they are determined from Eq. (5) considering the interface strength  $\sigma_{max} = 5.7$  MPa and the strain energy release rate  $G_I = 0.56$  N/mm for the present material.

### 3.3.3. Numerical results and comparison

The numerical DCB test is performed using the two specimens involving 40000 DE and 60000 DE. Constant and opposite

displacements are applied to the set of DE located at the left end side of ply-1 and ply-2 respectively, Figs. 11 and 12. Dual force  $P$  on the previous DE set results from DEM calculations by satisfying the equilibrium equations.

Firstly, the numerical (from DEM calculations) and analytical (from Eq. (10) and Eq. (11)) curves of macroscopic responses  $P = P(\Delta)$  and  $a/L = a/L(\Delta)$  are respectively plotted on Fig. 14(a) and Fig. 14(b). In comparison with the analytical beam model, a rather good trend can be observed. Numerical results underestimate both the apparent stiffness  $\frac{P}{2\Delta}$  of the specimens in the elastic stage and the  $P$  force corresponding to the beginning of the degradation of the interface, Fig. 14. After the damage initiation, numerical and analytical results match well. The implemented cohesive bonds at interface allow to correctly capture the interface degradation leading to a progressive decrease of the force  $P$  during the crack propagation. When the crack stops at the right end of specimens (ply-1 and ply-2 are fully separated at interface), specimens look like two separated beams (each ply is a beam) and then, the evolution of  $P = P(\Delta)$  increases linearly again. This is also quite well captured by present DEM. Moreover, the crack propagation  $a/L = a/L(\Delta)$ , Fig. 14(b), is correctly simulated exhibiting a higher non linearity compared to the analytical solution.

Secondly, the microscopic behavior at the interface can be assessed thanks to the DEM modeling. When the crack propagates, a process zone is visible ahead the tip, Fig. 16. This is the zone where the cohesive contact laws implemented between DE at interface are activated. As  $\Delta$  gradually grows, the closest cohesive contact bonds of crack tip rapidly evolve in the softening part of the cohesive law until they break. Thus, the loss of contact occurs and the crack propagates. Fig. 15(a) illustrates the process zone pointing out the zone where the cohesive contact bonds progress in the softening part (ie for which  $u_n$  is between  $u_n^e$  and  $u_n^p$ , Fig. 8(a)) and the one where they progress in the elastic part (ie for which  $u_n$  is between 0 and  $u_n^e$ , Fig. 8(a)). Fig. 15(b) shows the evolution of the process zone length when  $\Delta$  grows. It reveals that this length is almost constant as the crack propagates, Fig. 16.

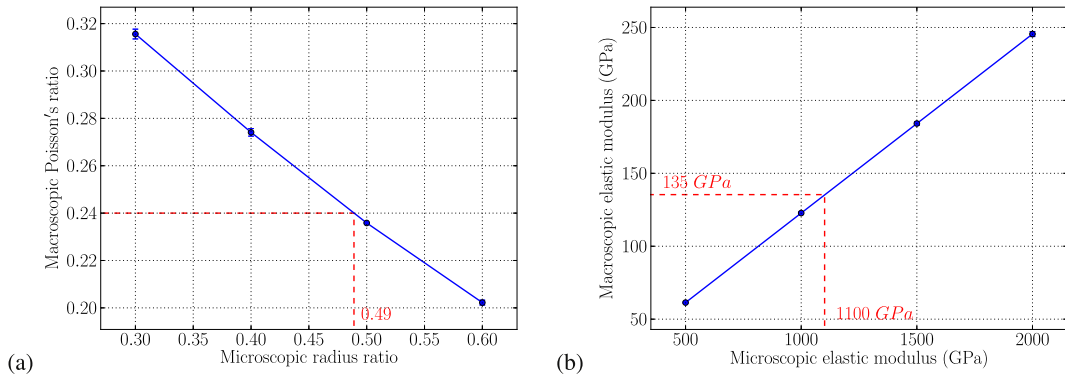


Fig. 13. Calibration curves for present material. (a) Radius ratio  $\tilde{r}_\mu$  calibration and (b) microscopic Young's modulus  $E_\mu$  calibration.

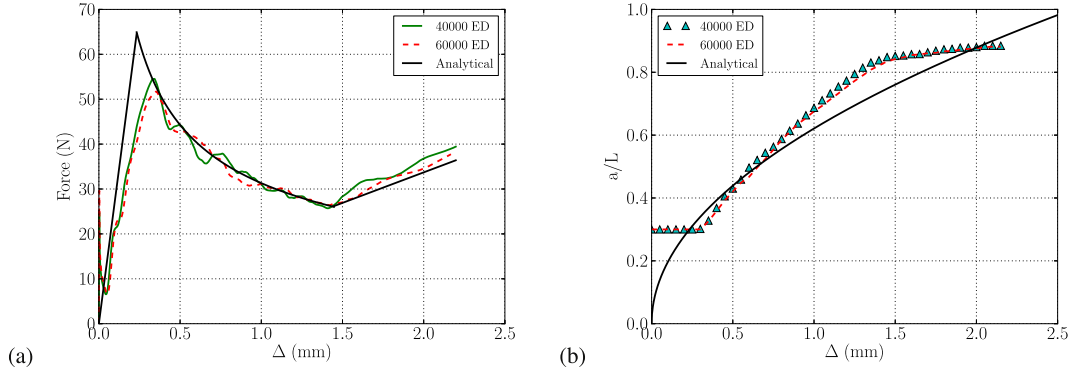


Fig. 14. (a) Load-displacement curves and (b) crack length-displacement curves in the DCB test.

Concerning the numerical convergency, Figs. 14 and 15(b) prove that suitable results can already be achieved with 40000 DE. Nevertheless, a smoother  $P = P(\Delta)$  curve, Fig. 14(a), can be obtained with 60000 DE. But the reality may not be so smooth due to local stick-slip behavior at interface. Such a behavior could be captured by the present DEM. Present results encourage the authors to experiment a DCB test.

#### 4. Simulation of transverse traction on a single-fiber composite specimen

The cohesive contact models (CCM) are now implemented at the interface between fiber and matrix to study the interface debonding. The simulation is based on the work of Alfaro et al. [1] in which a specimen made of a single fiber embedded in an epoxy resin block is subjected to a transverse tensile loading (Fig. 17). In this section, the effect of the ratio between the interface strength and matrix strength and the effect of the initial default on both the matrix cracks and debonding initiation and propagation are discussed. The influence of the discretization level on the numerical results is also analyzed. The composite material used is glass fiber with epoxy matrix. The mechanical properties of the components are summarized in Table 2.

##### 4.1. Specimen creation

The geometry of specimen and the loading are presented in Fig. 17(a). The diameter of glass fiber is  $10 \mu\text{m}$ . The specimen is a cube of dimensions  $28 \mu\text{m} \times 28 \mu\text{m} \times 28 \mu\text{m}$ . The fiber volume fraction is  $V_f = 0.1$ . A uniform displacement  $u$  is imposed at the right and left edges of specimen. Fig. 17(b) shows the single-fiber

specimen modeled with DE following the procedure described in Section 2.2. The fiber DE are firstly positioned (so as superimposed) in the middle of the cube. The DE overlapping is 90%. The cubic resin block is then filled in accordance with the filling procedure (see Section 2.2 and Fig. 5).

##### 4.2. Calibration of microscopic parameters

In this test, the matrix DE are connected by the cohesive beams whereas the fiber DE are connected by the spring links (Fig. 7(b)). The interface fiber/matrix is modeled by the cohesive contact models (CCM) as mentioned above.

For the epoxy matrix, supposed to be brittle elastic, the microscopic parameters of the cohesive beams ( $\tilde{r}_\mu, E_\mu, \nu_\mu$ ) are identified by the calibration procedure, as in the DCB test (Section 3.3.2). Knowing  $\tilde{r}_\mu, E_\mu, \nu_\mu$ , the microscopic failure stress  $\sigma_\mu$  is determined for both *BBF* and *RDEF* criteria, see Section 2.3.2. from a tensile test on a cylindrical sample (as for the elastic calibration) [48]. The microscopic parameters issued from calibration are listed in Table 3.

For the glass fiber, the DE are superimposed and connected by the spring links (Fig. 18b). The stiffness  $k_n$  of a spring  $n$  can be easily related to the stiffness  $K$  of the fiber, Eq. (12):

$$\frac{1}{K} = \sum_{n=1}^N \frac{1}{k_n} \quad K = ES/L \quad (12)$$

where  $N$  is the number of springs,  $E$  is the fiber Young's modulus,  $S = \pi R_f^2$  is the cross-section of the fiber with  $R_f$  its radius and  $L$  denotes the fiber length (Fig. 18(a)).

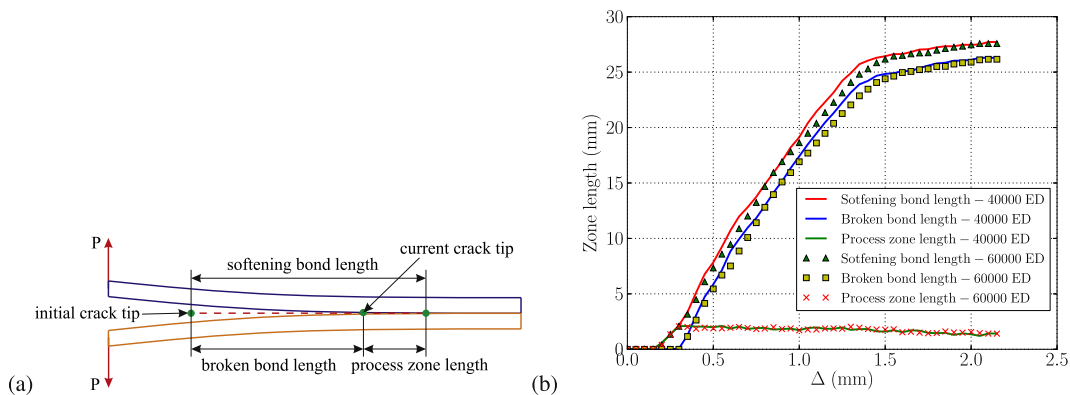


Fig. 15. (a) Distinction of damaged zones (b) damaged zone lengths in DEM.

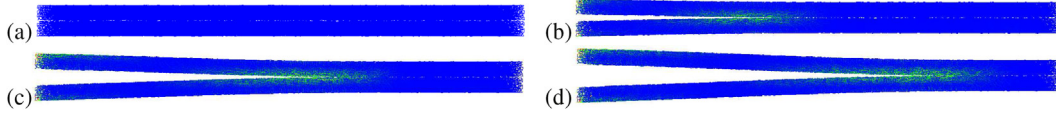


Fig. 16. Propagation of process zone at (a)  $\Delta = 0(mm)$ , (b)  $\Delta = 0.29(mm)$ , (c)  $\Delta = 0.73(mm)$  and (d)  $\Delta = 1.05(mm)$ .

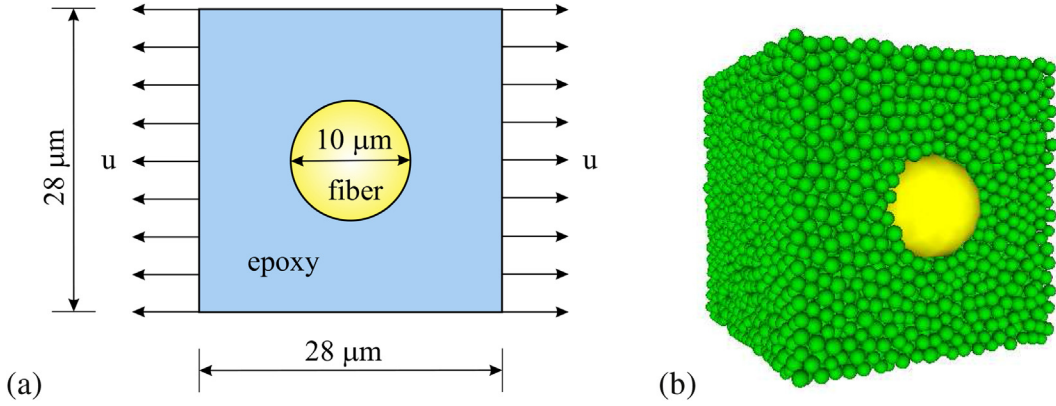


Fig. 17. Configuration of single-fiber test in (a) continuous media (b) discrete media.

Table 2

Material properties of the fiber-epoxy specimen.

Fiber Young's modulus (glass)	86.9 GPa
Fiber Poisson's ratio	0.23
Fiber radius	5 $\mu m$
Matrix Young's modulus (epoxy)	3.9 GPa
Matrix Poisson's ratio	0.37
Matrix yield stress	50 MPa
Interface tensile strength	25 MPa
Interface shear strength	25 MPa
Interface elastic stiffness	10 <sup>8</sup> N/mm
Interface fracture energy release rate (mode I and mode II)	0.5 N/mm

For the interface glass/epoxy, CCM presented in Section 2.3.1 (Fig. 9(b)) is introduced. The contact surface between a fiber DE and a matrix DE is supposed to be equal to  $S \approx \pi R_1^2$ . The microscopic parameters of the cohesive contact model ( $u_n^e$ ,  $u_n^p$ ,  $F_n^c$ ) are determined from the Eq. (5) using an interface strength  $\sigma_{max}$  of 25 MPa, a strain energy release rate  $G_I$  of 0.5 N/mm and an interface elastic stiffness  $k_{int}^{elas}$  of 10<sup>8</sup> N/mm with  $k_{int}^{elas} = \frac{F_n^c}{u_n^p}$ . At this stage of work, these values have not been experimentally identified but extracted from the work of Alfaro et al. [1].

#### 4.3. Sensitivity to the mesh refinement

In order to study the influence of the discretization on the numerical results, three specimens corresponding respectively to a 'Coarse discretization', an 'Intermediate discretization' and a 'Fine discretization', Fig. 19 are considered. The number of fiber DE and matrix DE as well as the number of interfaces between the fiber and

Table 3

Calibration of microscopic parameter of epoxy matrix.

Matrix epoxy	$E$ (GPa)	$\nu$	$\sigma_M$ (MPa)	$\tilde{r}_\mu$	$\sigma_\mu$ (MPa)
Continuum properties $M$	3.9	0.37	50	–	–
Discrete properties $\mu$	429	0.3	–	0.19	–
with the BBF criterion					5700
with the RDEF criterion					162

matrix are listed in Table 4 for each specimen. The number of fiber DE is unchanged for the three specimens.

The numerical test consists in a transversal tensile loading by imposing a uniform displacement  $u$  on opposite edges of specimens, see Fig. 17(a). The interface strength  $\sigma_{max}$  between fiber and matrix is fixed to the value of 25 MPa. The two failure criteria, respectively BBF and RDEF, have been assessed, see section 2.3.2.

Fig. 20 presents the stress-strain curves obtained for the three specimens with the two failure criteria. Strain and stress values plotted are obtained by averaging the discrete values on the right section of specimen. Using BBF criterion or RDEF leads to distinct behavior. A more brittle behavior is observed using the BBF criterion. Moreover, numerical convergency is acceptable as the use of the specimen with the coarse mesh with this criterion. Using the RDEF criterion, the convergency is achieved from the intermediate discretization.

The crack is shown in Fig. 21 and Fig. 22 for the three discretization levels using the two failure criteria. It is represented by the DE in purple color for which the cohesive beams have been broken. As in the stress-strain curves, rather reproducible results are observed regardless mesh refinement with BBF criterion while the intermediate discretization seems to be the minimum necessary for convergency with RDEF criterion. In both cases, the tendency of the crack path is the same. Appearing in the middle of specimen, it globally propagates perpendicularly to the loading direction (transverse to the fibers). The crack totally passes through the specimen for  $\varepsilon = 0.018$  using BBF and for  $\varepsilon = 0.08$  using RDEF.

#### 4.4. Interface strength ratio

The traversal cracking highly depends on the ratio between the matrix strength  $\sigma_M$  and the fiber/matrix interface strength  $\sigma_I$ . The influence of this strength ratio on the failure process is studied hereafter. Two strength ratios are considered:  $\sigma_M/\sigma_I = 2$  and  $\sigma_M/\sigma_I = 0.5$ .  $\sigma_M$  remains constant and equal to 50 MPa, Table 3. The fine discretization specimen is used. In this section, the numerical results are presented using the RDEF criterion for matrix failure criterion. As mentioned in Ref. [17], the use of this criterion allows a

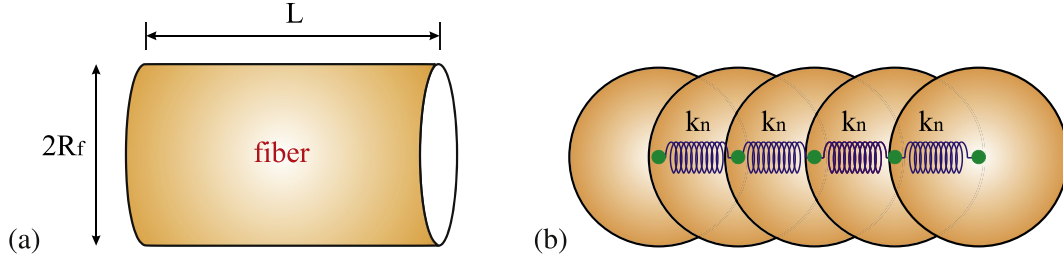


Fig. 18. Fiber modeling: continuous medium (a) and the spring link connected the DE of fiber in DEM (b).

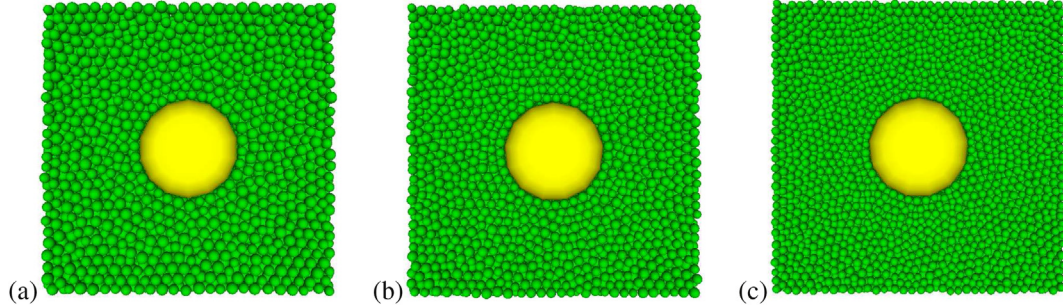


Fig. 19. Single-fiber composite specimens (a) coarse discretization (18835 ED), (b) intermediate discretization (27916 ED) (c) fine discretization (46004 ED).

**Table 4**  
Number of DE used for the three specimens.

Discretization	DE for fiber	DE for matrix	DE for fiber/matrix interface	Total
Coarse	25	18810	624	18835
Intermediate	25	27891	832	27916
Fine	25	45979	1167	46004

good representation of the macroscopic behavior but also of the microscopic one.

In the first case,  $\sigma_M/\sigma_I = 2$ , the interface strength is then lower than the matrix one. It is related to the crack path briefly described in the above section, Fig. 22. The crack propagation is now more discussed. Fig. 24 presents the broken cohesive beams (or bonds) in matrix during the failure process at different strain levels. Two types of cracks appear: cracks in matrix and debonding at the fiber/matrix interface. As  $\sigma_M/\sigma_I = 2$ , damage appears firstly at interface. Then, cracks initiate and propagate in matrix all around the interface. They mainly appear in the middle cross-section containing the fiber, perpendicular to the load direction. Cracks develop in this

cross section area till the final rupture of the specimen (see Fig. 23(b)).

Moreover, the force-displacement behavior is plotted in Fig. 23(a). The behavior is linear elastic until the displacement  $u = 21.10^{-5} \text{ mm}$  (corresponding to strain  $\epsilon = 0.015$ , see Fig. 20(b)). Then, a non-linear behavior is visible due to cracks appearance, Fig. 24(a,e). The maximum force is around  $42.10^{-3} \text{ N}$  obtained for  $u = 26.10^{-5} \text{ mm}$  (or strain  $\epsilon = 0.019$ , see also Fig. 24(b,f)). Then, the force decreases as interface damages progressively appear as well as cracks in matrix. It tends to zero very slowly because the failure strain is upper at interface than in matrix.

For  $\sigma_M/\sigma_I = 0.5$ , the interface strength is greater than the matrix one. Fig. 23(d) represents the crack path whereas the force-displacement is plotted in Fig. 23(a) for this case. As the interface is more resistant than in previous case, the slope of linear part of the force-displacement curve is higher until the maximum value of  $48.10^{-3} \text{ N}$ . Then, the force decreases more rapidly compared to the case with  $\sigma_M/\sigma_I = 2$ . It vanishes when the crack totally passes through the specimen at the approximative displacement value of  $u = 12.10^{-4} \text{ mm}$  (or strain  $\epsilon = 0.09$ ). As for  $\sigma_M/\sigma_I = 2$ , cracks initially appear in the matrix around the interface fiber/matrix area, then

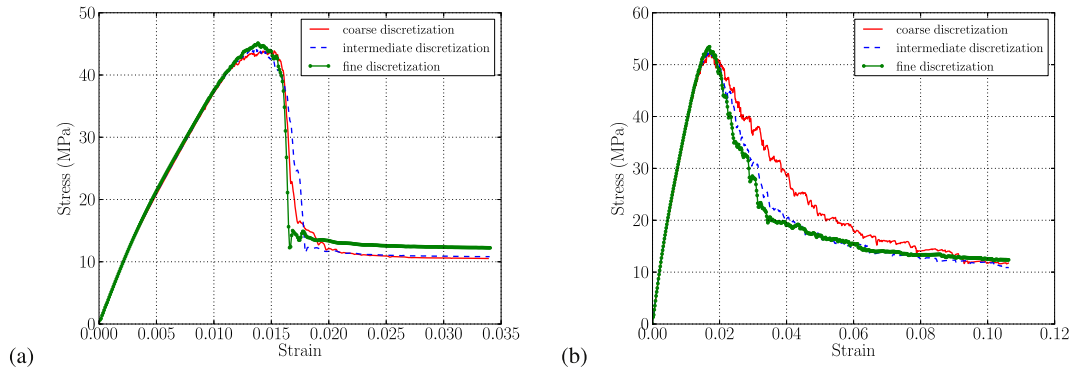


Fig. 20. Stress-strain curves for the three specimens (a) using BBF criterion (b) using RDEF criterion.

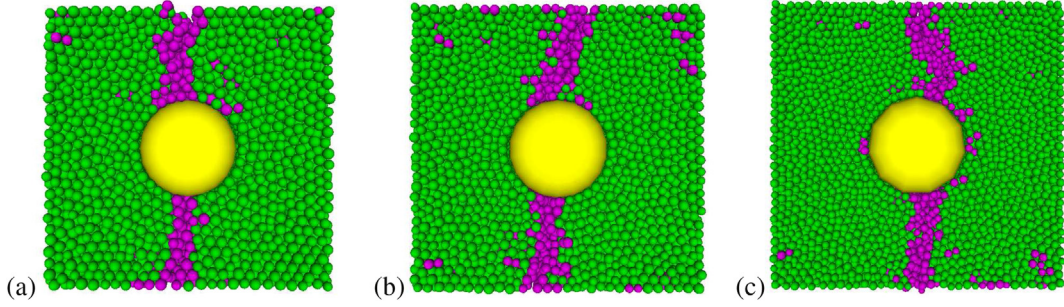


Fig. 21. Path of the crack,  $\varepsilon = 0.018$ , using BBF criterion (a) with the coarse discretization (b) with the intermediate discretization (c) with the fine discretization.

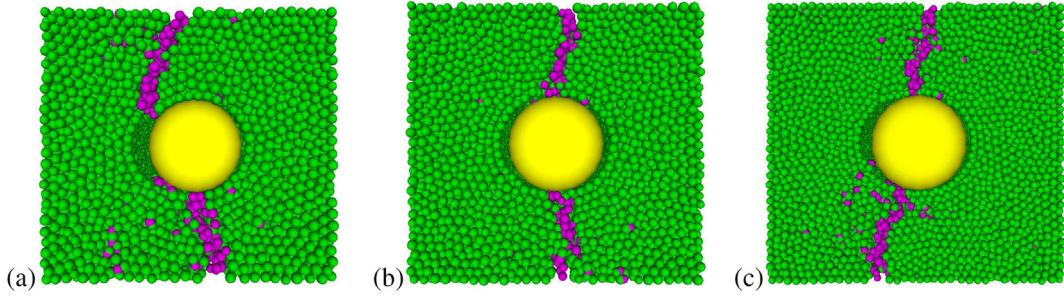


Fig. 22. Path of the crack,  $\varepsilon = 0.08$ , using RDEF criterion (a) with the coarse discretization, (b) with the intermediate discretization and (c) with the fine discretization.

propagate along the cross section, perpendicularly to the load direction, Fig. 25.

For both  $\sigma_M/\sigma_I = 2$  and  $\sigma_M/\sigma_I = 0.5$ , consistent and encouraging results are obtained in comparison with results obtained with the Finite Element Modeling (FEM) [1], Fig. 23(c), (e). A good trend of microscopic cracks path is observed. For  $\sigma_M/\sigma_I = 2$ , cracks develop in the middle cross-section, firstly in the matrix and than at the fiber/matrix interface bypassing the fiber. In contrast, cracks appear only in the matrix for  $\sigma_M/\sigma_I = 0.5$ . Concerning the macroscopic force response, the same elastic part until the maximum force is obtained using the two methods DEM and FEM (Fig. 23(a)). However, a significant difference in trend is observed for the force evolution during the cracks propagation. A more brittle behavior occurs with DEM. This result is explained by the different matrix failure criterion used in each simulation methods. In DEM, the matrix follows a

linear fracture model (*RDEF* criterion) whereas a piecewise linear model (the same than used at interfaces) is used in FEM. So, the comparison is not proper beyond the linear part.

#### 4.5. Default and cracks growth

The influence of initial defaults in matrix on the macroscopic response is now studied. Two porosities values are considered:  $P_r = 2\%$  and  $P_r = 5\%$  for the two strength ratio  $\sigma_M/\sigma_I = 2$  and  $\sigma_M/\sigma_I = 0.5$ . In the present discrete domain, an initial default is implemented by specifying that a set of the cohesive beam is free of all efforts. Yellow cohesive beams in Fig. 26 describe one possible configuration of a distribution of defaults for  $P_r = 2\%$ .

In this section, the capacity of default implementation is mainly aimed. Even if it is not the best to capture the mechanisms

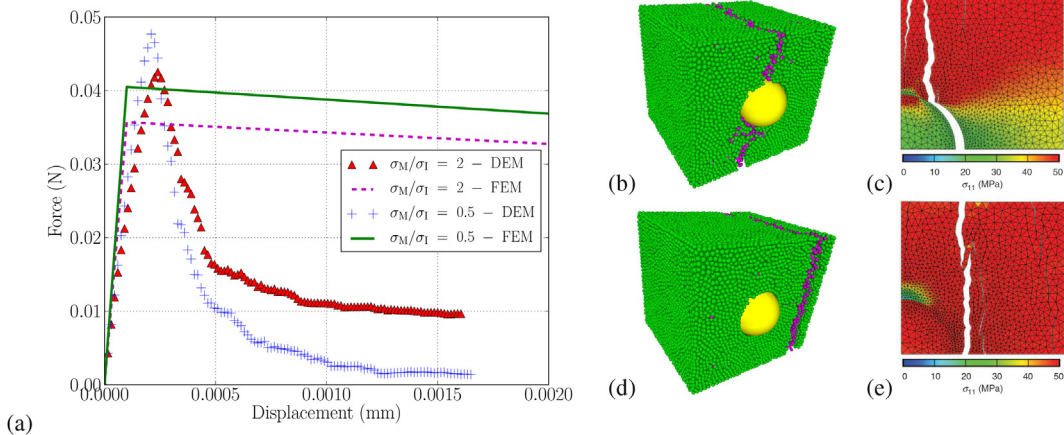
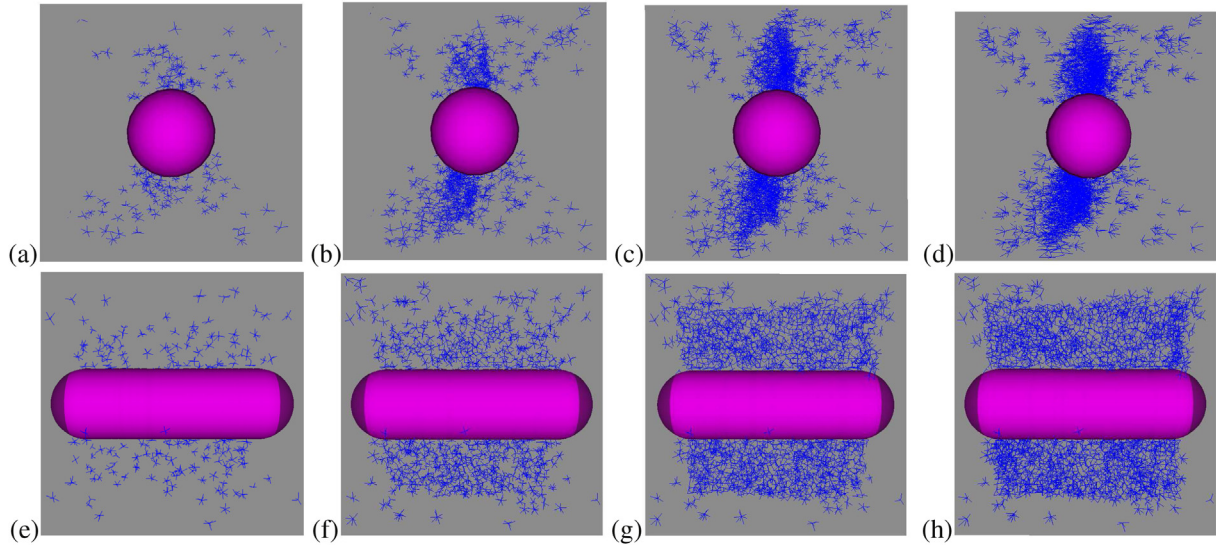


Fig. 23. (a) Compare the evolution of force-displacement with the Finite Element Modeling [1] for  $\sigma_M/\sigma_I = 2$  and  $\sigma_M/\sigma_I = 0.5$ , Crack path for (b)  $\sigma_M/\sigma_I = 2$  and (c) the equivalent in FEM, (d) for  $\sigma_M/\sigma_I = 0.5$  and (e) the equivalent in FEM.



**Fig. 24.** Failure process for  $\sigma_M/\sigma_I = 2$ . Representation of the broken bonds in matrix (blue color) for different macroscopic values of strain. (a,e)  $\varepsilon = 15.10^{-3}$ , (b,f)  $\varepsilon = 19.10^{-3}$ , (c,g)  $\varepsilon = 27.10^{-3}$ , (d,h)  $\varepsilon = 53.10^{-3}$ . (a,b,c,d) and (e,f,g,h) illustrate respectively the face and side views (For interpretation of the references to color in this figure legend, the reader is referred to the web version of this article).

occurring at microscopic scale, the *BBF* criterion is essentially used here for convenience.

The macroscopic stress-strain curves obtained are plotted in Fig. 27(a) for  $\sigma_M/\sigma_I = 2$  and in Fig. 27(b) for  $\sigma_M/\sigma_I = 0.5$ , assigning the porosity value at  $P_r = 0\%$ ,  $P_r = 2\%$  and  $P_r = 5\%$ . For  $\sigma_M/\sigma_I = 2$ , no significant difference on the stress-strain curve is observed with  $P_r = 0\%$  and  $P_r = 2\%$ . However, the maximum macroscopic stress decreases of 22% when the porosity goes from  $P_r = 0\%$  to  $P_r = 5\%$ . Moreover, the non linear behavior seems to become less brittle when the porosity increases.

For  $\sigma_M/\sigma_I = 0.5$ , the same tendency can be observed. Nevertheless, the macroscopic stress-strain curve is more sensitive to the low porosity. Indeed, a decrease of 13% on the maximum stress value is obtained from  $P_r = 2\%$ . It is unchanged for  $P_r = 5\%$ . The softening effect for this porosity is not as influential on the

macroscopic behavior as in the previous case with  $\sigma_M/\sigma_I = 2$ , where the interface debonding participates significantly on the crack propagation process. On the contrary, the crack mainly propagates in the matrix when  $\sigma_M/\sigma_I = 0.5$ .

Fig. 28 illustrates the failure process for the porosity  $P_r = 2\%$  and the strength ratio  $\sigma_M/\sigma_I = 0.5$ . Cracks initially appears around the defaults before propagating through the matrix perpendicularly to the load direction.

### 5. Simulation of transverse traction on a multi-fibers composite specimens

To complete the failure study, a transverse traction test in 3D on a so-called multi-fibers composite specimen, or Statistical Elementary Volume (SEV), is considered in this section. The

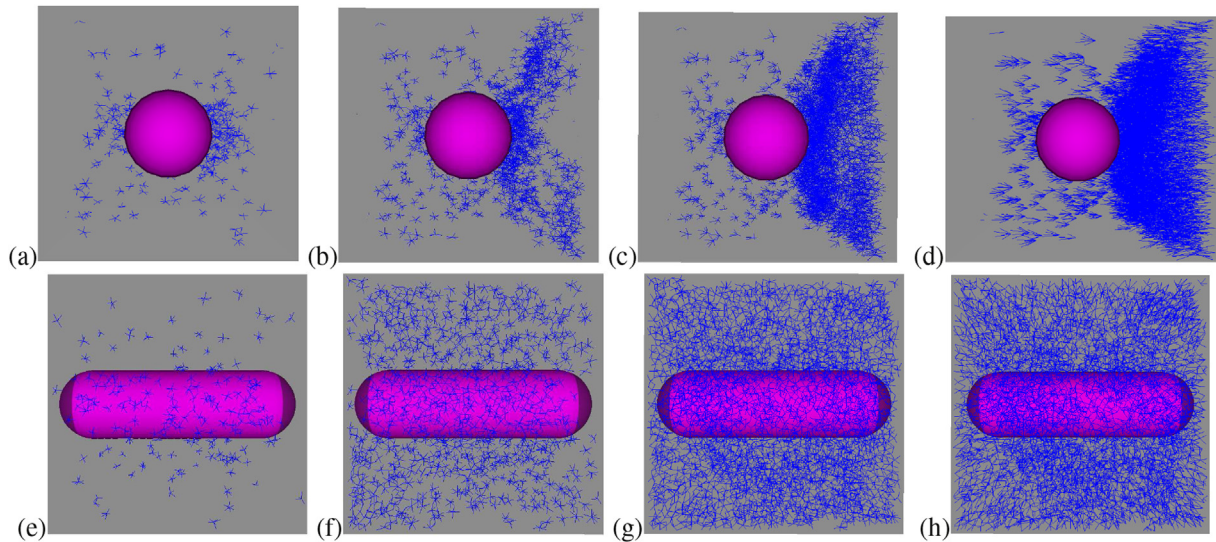


**Fig. 25.** Failure process for  $\sigma_M/\sigma_I = 0.5$ . Representation of the broken bonds in matrix (blue color) for different macroscopic values of strain. (a,e)  $\varepsilon = 14.10^{-3}$ , (b,f)  $\varepsilon = 17.10^{-3}$ , (c,g)  $\varepsilon = 35.10^{-3}$ , (d,h)  $\varepsilon = 53.10^{-3}$ . With face views (a,b,c,d) and side views (e,f,g,h) (For interpretation of the references to color in this figure legend, the reader is referred to the web version of this article).

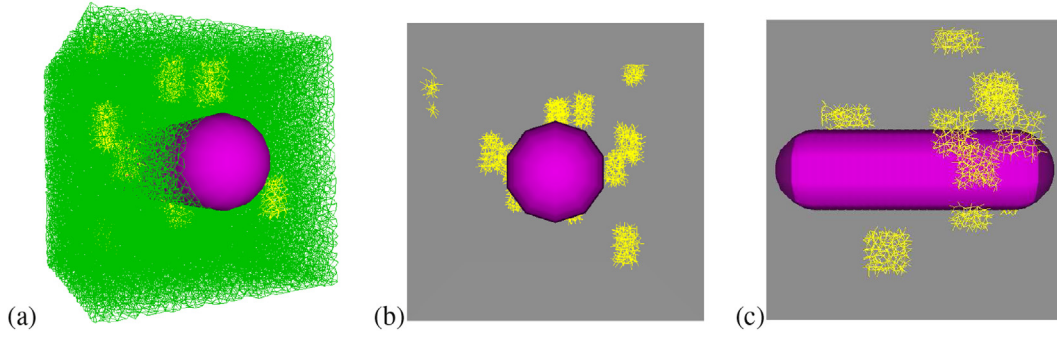


**Fig. 26.** Configuration of defaults (yellow beam) in specimen for  $P_r = 2\%$  displayed (a) in 3D (b) in face views (c) in side views (For interpretation of the references to color in this figure legend, the reader is referred to the web version of this article.)

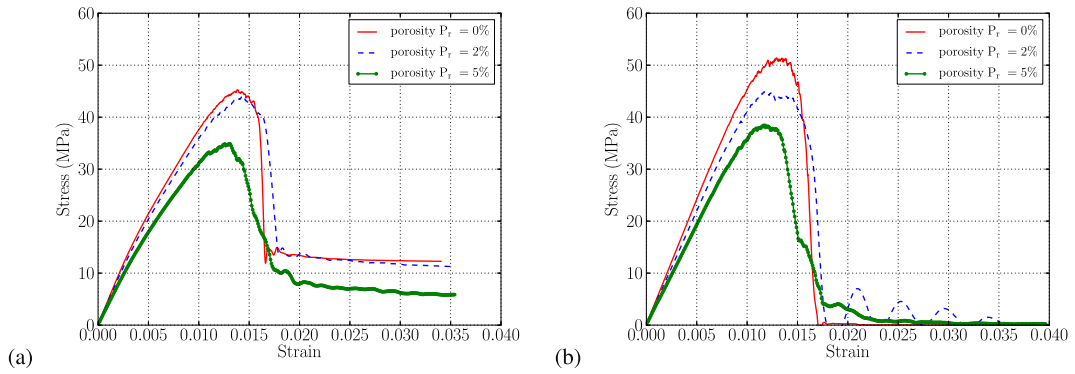


**Fig. 27.** Evolution of stress-strain for  $P_r = 0\%$ ,  $P_r = 2\%$  and  $P_r = 5\%$  with: (a)  $\sigma_M/\sigma_f = 2$  (b)  $\sigma_M/\sigma_f = 0.5$ .

specimen is a cube of side dimensions  $125 \mu\text{m}$  (Fig. 29). It is made of fibers randomly placed in the matrix. The diameter of fibers is  $10 \mu\text{m}$ . The influence of the fiber volume fraction  $V_f$  and the ratio between the matrix strength  $\sigma_M$  and the fiber/matrix interface strength  $\sigma_f$  on both microscopic and macroscopic responses will be investigated. A transverse uniform displacement  $u$  is imposed at opposite edges of the specimen. The material properties are referenced in Table 2. To prevent from edge effects in the numerical

simulation, unbreakable resin bands (mazarine color) have been added at opposite edges of the specimen (Fig. 29)(b). As for the single-fiber composite specimen (see Section 4), the cohesive contact laws are implemented at fiber/matrix interfaces and the RDEF criterion used for failure of matrix.

Three fiber volume fractions  $V_f = 0.1, 0.3$  and  $0.4$  are considered, Fig. 30. The number of DE used for fiber, matrix and fiber/matrix interface is mentioned in Table 5 for each specimen. For each  $V_f$ , two

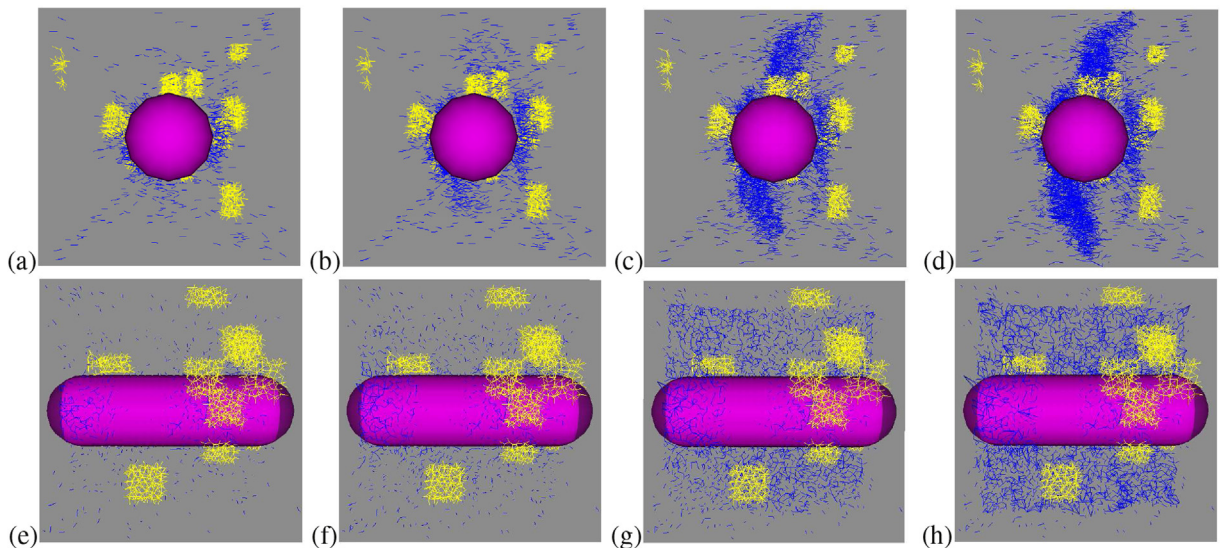


**Fig. 28.** Failure process for  $P_r = 2\%$  and  $\sigma_M/\sigma_f = 0.5$ . Broken bonds in matrix (blue color) for different macroscopic values of strain: (a,e)  $\epsilon = 14.10^{-3}$ , (b,f)  $\epsilon = 16.10^{-3}$ , (c,g)  $\epsilon = 17.10^{-3}$ , (d,h)  $\epsilon = 19.10^{-3}$  displayed in (a,b,c,d) face views and (e,f,g,h) side views.

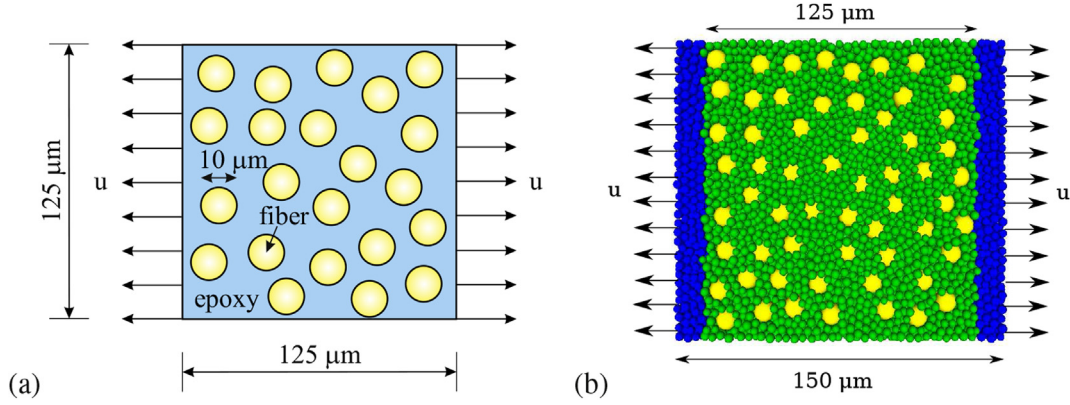


Fig. 29. Geometry of multi-fibers composite specimen with  $V_f=0.3$ , (a) continuous media (b) discrete media.

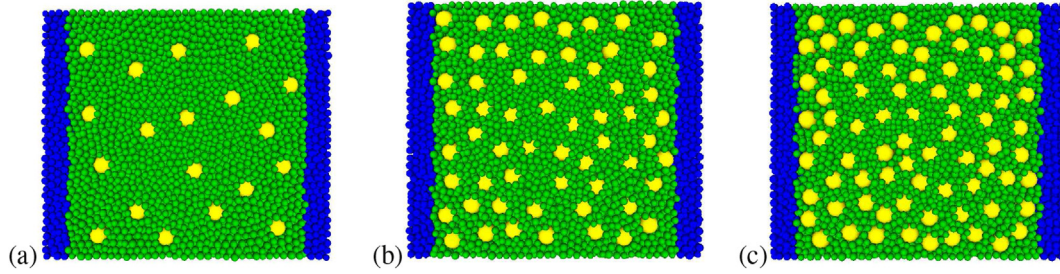


Fig. 30. Geometry of specimens using three fiber volume fractions: (a)  $V_f=0.1$  (b)  $V_f=0.3$ , (c)  $V_f=0.4$ .

strength ratios  $\sigma_M/\sigma_I=2$  and  $\sigma_M/\sigma_I=0.5$  are considered. The matrix strength is fixed to  $\sigma_M=50$  MPa, Table 3.

For  $\sigma_M/\sigma_I=2$ , the crack path is illustrated for  $V_f=0.1$ ,  $V_f=0.3$  and  $V_f=0.4$  at the displacement  $u=115.10^{-4}$  mm (or strain  $\epsilon=0.184$ ), Fig. 31. Cracks in matrix (in purple color) and debonding at fiber/matrix interfaces can be depicted. For the lowest value of  $V_f$ , the matrix mainly governs the crack path and the failure occurs at the middle of the specimen. For higher values of  $V_f$ , the crack path seems to be more influenced by the debonding of nearby fibers edges.

Concerning the macroscopic force-displacement curves plotted in Fig. 33(a), the slope of the linear part highly decreases as the fiber volume fraction increases. Moreover, the maximum force, obtained for approximately  $u=20.10^{-4}$  mm for all  $V_f$  values, significantly decreases as  $V_f$  increases.

For  $\sigma_M/\sigma_I=0.5$ , the crack path is illustrated in Fig. 32 for all  $V_f$  tested values. The interface strength being greater than the matrix one, the crack mainly develops in the matrix and the fracture occurs close to the edge. The force-displacement curves plotted in Fig. 33(b) exhibit steeper slopes than that observed with  $\sigma_M/\sigma_I=2$ , Fig. 33(a). For the lowest values of  $V_f$ , i.e.  $V_f=0.1$  and  $V_f=0.3$ , the stiffness matrix is well recovered in the linear part. Moreover, the macroscopic force decreases rapidly after its maximum value. Thus, the matrix behavior approaching a rather brittle behavior is properly restored. On the other hand, broken elements (in white color),

not visible when  $\sigma_M/\sigma_I=2$ , occur at fiber/matrix interfaces at strain  $\epsilon=0.184$  (Fig. 32). This is explained by an upper value of  $u^p$  used in the cohesive model (Fig. 8) for the present ratio  $\sigma_M/\sigma_I=0.5$ , the energy release rate remaining the same for the two  $\sigma_M/\sigma_I$  ratios.

Compared with the FEM results, a similar linear part is obtained in both case  $\sigma_M/\sigma_I=2$  (Fig. 33)(a) and  $\sigma_M/\sigma_I=0.5$  (Fig. 33)(b) for  $V_f=0.1$  and  $V_f=0.3$ . However, DEM exhibits a more brittle behavior than FEM. The reason is the same explained in the single-fiber composite case (Section 4.4).

## 6. Conclusions and prospects

An original DEM approach is presented. In continuation of previous works in Refs. [17], the present paper confirms the ability of the method to model in 3D the damages and cracks growth in composite materials. Cohesive contact laws are implemented for studying the delamination between plies as well as the debonding between fibers and matrix. In order to better describe the adhesion at fiber-matrix interfaces and to reduce the discrete element number and thus the computation time, bi-disperse media are introduced in this work.

In the first simulation, the delamination problem is addressed considering the DCB test. The cohesive contact is then introduced at the interface between plies. Satisfactory macroscopic responses are achieved in comparison with the analytical results available for DCB test. Also, crack growth and process zone can be well captured. For transverse traction simulations on respectively a single-fiber and a multi-fibers (or VSE) composite specimen, the fiber-matrix debonding and the matrix cracking can be tracked thanks to the implemented cohesive contact laws and the *BBF* and *RDEF* failure criteria for matrix already experimented in Ref. [17]. The result tendency by varying the ratio between the matrix strength and the interface strength and the fiber volume fraction (for SEV) is rather

Table 5  
Discrete elements number of different fiber volume fraction.

Volume fraction	DE for fiber	DE for matrix	DE for fiber/matrix interface	Total number of DE
$V_f=0.1$	456	38231	4696	38687
$V_f=0.3$	1416	28959	12902	30375
$V_f=0.4$	1896	23616	11537	25512

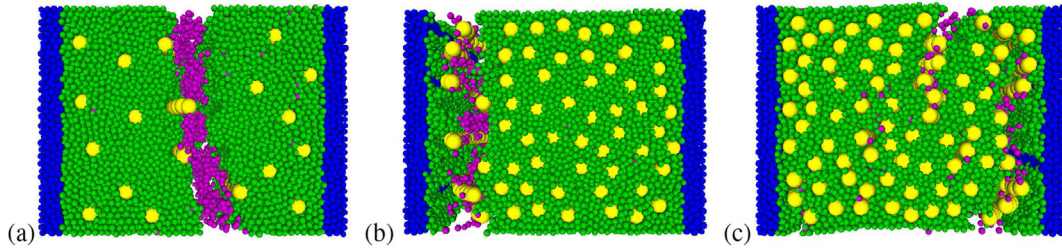


Fig. 31. Crack path in composite specimen for  $\sigma_M/\sigma_I=2$  at strain  $\epsilon = 0.184$  for (a)  $V_f=0.1$ , (b)  $V_f=0.3$  (c)  $V_f=0.4$ .

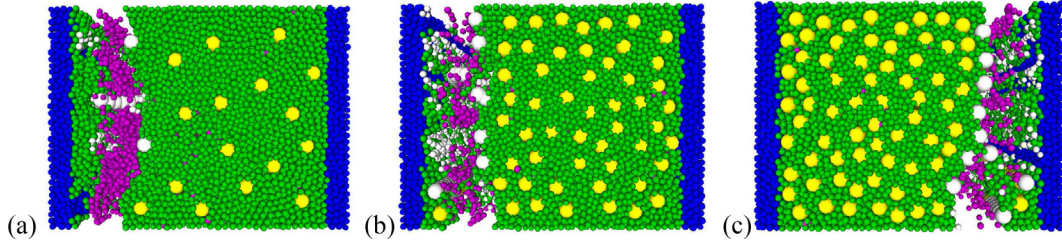


Fig. 32. Crack path in composite specimen for  $\sigma_M/\sigma_I=0.5$  at strain  $\epsilon = 0.184$  for (a)  $V_f=0.1$ , (b)  $V_f=0.3$  (c)  $V_f=0.4$ .

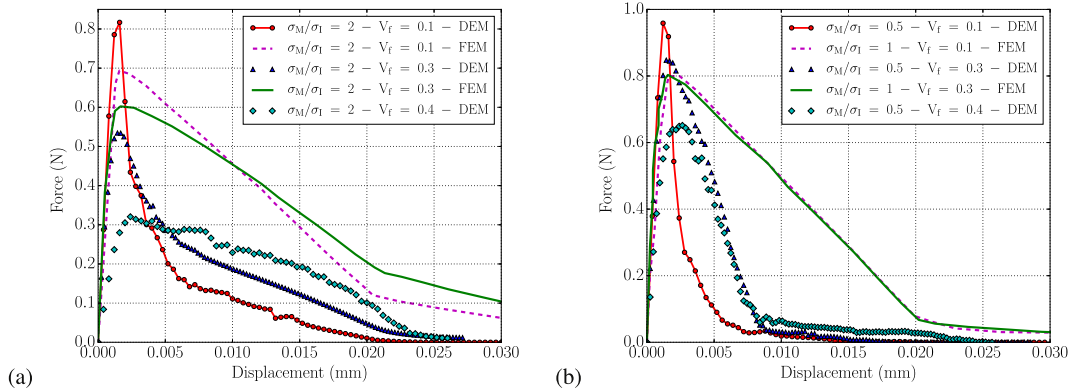


Fig. 33. Compare the evolution of force-displacement curve with FEM [1] at  $V_f=0.1$ ,  $V_f=0.3$  and  $V_f=0.4$  for (a)  $\sigma_M/\sigma_I=2$  and (b)  $\sigma_M/\sigma_I=0.5$ .

good compared with the Finite Element Method [1] both on the macroscopic responses (force-displacement curves) and the damage mechanisms occurring at microscopic scale.

In order to further improve the quantitative results, the authors are now working on both experimental and numerical tests to identify the mechanical parameters needed by the cohesive contact laws. A fragmentation testing on  $0^\circ$  single yarn composite specimen [49] is particularly addressed to achieve those parameters in case of shear contact. About the normal contact, authors are interesting in the laser shock performed on a block of resin with an embedded yarn. A tension zone can be locally generated using this process. Then, by having experimentally both macroscopic and microscopic diagnosis, the mechanical parameters needed by the normal cohesive contact laws could be identified by an inverse approach. However, a particular attention should be focused on the strain rate effect.

## References

- [1] Cid Alfaro MV, Suiker ASJ, De Borst R. Transverse failure behavior of fiber-epoxy systems. *J Compos Mater* 2010;44(12):1493–516.
- [2] Ecault R, Boustie M, Touchard F, Pons F, Berthe L, Chocinski-Arnault L, et al. A study of composite material damage induced by laser shock waves. *Compos Part A* 2013;53:54–64.
- [3] Gamstedt EK, Sjogren BA. Micromechanisms in tension-compression fatigue of composite containing transverse plies. *Compos Sci Technol* 1999;59:167–78.
- [4] Whitney JM, Nuismer RJ. Stress fracture criteria for laminated composites containing stress concentrations. *J Compos Mater* 1974;8:253–65.
- [5] Kim RY, Soni SR. Experimental and analytical studies on the onset of delamination in laminated composites. *J Compos Mater* 1984;18:70–80.
- [6] Zou Z, Reid SR, Li S, Soden PD. Application of a delamination model to laminated composite structures. *Compos Struct* 2002;56(4):375–89.
- [7] Schoepner GA, Pagano NJ. Stress fields and energy release rates in cross-ply laminates. *Int J Solids Struct* 1998;11:1025–55.
- [8] Krueger R, Minguet PJ, OBrien TK. A method for calculating strain energy release rates in preliminary design of composite skin/stringer debonding under multi-axial loading. *NASA Tm* 1999:209365.
- [9] Krueger R, OBrien TK. A shell/3D modeling technique for the analysis of delaminated composite laminates. *Compos Part A* 2001;32:25–44.
- [10] Shen F, Lee KH, Tay TE. Modeling delamination growth in laminated composite. *Compos Sci Technol* 2001;61:1239–51.
- [11] Xie D, Biggers SB. "Strain energy release rate calculation for a moving delamination front of arbitrary shape based on the virtual crack closure technique. Part I: formulation and validation. *Eng Fract Mech* 2006;73:771–85.
- [12] Xie D, Biggers SB. Strain energy release rate calculation for a moving delamination front of arbitrary shape based on the virtual crack closure technique.

- Part II: Sensitivity study on modeling detail. *Eng Fract Mech* 2006;73:786–801.
- [13] Camanho PP, Davila CG, De Moura MF. Numerical simulation of mixed-mode progressive delamination in composite materials. *J Compos Mater* 2003;37:1415–38.
- [14] Crisfield MA, Alfano G. Finite element interface models for the delamination analysis of laminated composites: mechanical and computational issues. *Int J Numer Methods Eng* 2000;50:1701–36.
- [15] Pinho ST, Iannucci L, Robinson P. Formulation and implementation of decohesion elements in an explicit finite element code. *Compos A Appl Sci Manuf* 2006;37:778–89.
- [16] Paul WH, Stephen RH. Cohesive zone length in numerical simulations of composite delamination. *Eng Fract Mech* 2008;75:4774–92.
- [17] Maheo L, Dau F, André D, Charles JL, Iordanoff I. A promising way to model cracks in composites using a discrete element method. *Compos part B* 2015;71:193–202.
- [18] Yang D, Sheng Y, Ye J, Tan Y. Discrete element modeling of the microbond test of fiber reinforced composite. *Comput Mater Sci* 2010;49:253–9.
- [19] Yang D, Sheng Y, Ye J, Tan Y. Modeling progressive delamination of laminated composites by discrete element method. *Comput Mater Sci* 2011;50:858–64.
- [20] Mohammad JK, Ahmed K. Modeling tensile response of fiber-reinforced polymer composites using discrete element method. *Polym Compos* 2013;34:877–86.
- [21] Wittel FK, Schulte-Fischedick J, Kun F, Kröplin BH, Frieb M. Discrete element simulation of transverse cracking during the pyrolysis of carbon fibre reinforced plastics to carbon/carbon composites. *Comput Mater Sci* 2003;28:1–15.
- [22] Wittel FK, Kun F, Kröplin BH, Herrmann HJ. A study of transverse ply cracking using a discrete element method. *Comput Mater Sci* 2003;28(3–4):608–19.
- [23] Cundall PA, Strack ODL. A discrete numerical model for granular assemblies. *G* 1979;29:47–65.
- [24] Calvetti F, Viggiani G, Tamagnini CA. Numerical investigation of the incremental non-linearity of granular soils. *Riv. Ital. di Geotec. 2003*;3:11–29.
- [25] Cleary P. Modeling comminution devices using DEM. *Int J Numer Methods Geomechanics* 2001;25:83–105.
- [26] Jensen RP, Plesha ME, Edil T, Bosscher PJ, Kahla NB. DEM simulation of particle damage in granular media-structure interfaces. *Int J Geomechanics* 2001;1(1):21–39.
- [27] Sibille L, Nicot F, Donzé FV, Darve F. Material instability in granular assemblies from fundamentally different models. *Int J Numer Anal Methods Geomechanics* 2007;31:457–81.
- [28] Takada S, Hassani N. Earthquake resistant engineering structures. Analysis of compression failure of reinforced concrete by the modified distinct element method, vol. 23. Computational Mechanics Publications; 1996.
- [29] Matsuda Y, Iwase Y. Numerical simulation of rock fracture using three-dimensional extended discrete element method. *Earth Planets Space* 2002;54:367–78.
- [30] Potyondi DO, Cundall PA. A bonded-particle model for rock. *Int J Rock Mech Min Sci* 2004;41(8):1329–64.
- [31] Carmona HA, Wittel FK, Kun F, Herrmann HJ. Fragmentation processes in impact of spheres. *Phys Rev* 2008;77(5):051302.
- [32] Le BD, Koval G, Chazallon C. Discrete element approach in brittle fracture mechanics. *Eng Comput* 2013;30(2):263–76.
- [33] Tavares FA, Plesha ME. Discrete element method for modelling solid and particulate materials. *Int J Numer methods Eng* 2007;70:379–404.
- [34] Kun F, Herrmann HJ. A study of fragmentation processes using a discrete element method. *Comput Methods Appl Mech Eng* 1996;138(1–4):3–18.
- [35] Delaplace A, Desmorat R. Discrete 3d model as complimentary numerical testing for anisotropic damage. *Int J Fract* 2007;148:115–28.
- [36] Sheng Y, Yang D, Ye J, Tan Y. Modeling progressive delamination of laminated composites by discrete element method. *Compos Sci Technol* 2010;70:2093–101.
- [37] Schlangen E, Garboczi EJ. New method for simulating fracture using an elastically uniform random geometry lattice. *Int J Eng Sci* 1996;34(10):1131–44.
- [38] Schlangen E, Garboczi EJ. Fracture simulations of concrete using lattice models: computational aspects. *Eng Fract Mech* 1997;57(2–3):319–32.
- [39] Jean M, Desmorat R. The non-smooth contact dynamics method. *Comput Appl Mech Eng* 1999;177(3–4):235–57.
- [40] André D, Charles JL, Iordanoff I, Nauport J. The GranOO workbench, a new tool for developing discrete element simulations, and its application to tribological problems. *Eng Softw* 2014;74:40–8.
- [41] Eberly D. Game physics. 2010.
- [42] André D, Charles JL, Iordanoff I, Nauport J. Discrete element method to simulate continuous material by using the cohesive beam model. *Comput Methods Appl Mech Eng* 2012;231–216:113–25.
- [43] Rougier E, Munjiza A, John NWM. Numerical comparison of some explicit time integration schemes used in DEM, FEM/DEM and molecular dynamics. *Int J Numer methods Eng* 2004;62:856–79.
- [44] Xie D, Waas AM. Discrete cohesive zone model for mixed-mode fracture using finite element analysis. *Eng Fract Mech* 2006;73(13):1783–96.
- [45] Nishikawa M, Okabe T, Takeda N. Numerical simulation of interlaminar damage propagation in CFRP cross-ply laminates under transverse loading. *Eng Fract Mech* 2007;44(10):3101–13.
- [46] Camborde F, Mariotti C, Donzé FV. Numerical study of rock and concrete behaviour by discrete element modeling. *Comput Geotechnics* 2000;27(4):225–47.
- [47] Jebahi M, André D, Dau F, Charles JL, Iordanoff I. Simulation of vickers indentation of silica glass. *J Non Cryst Sol* 2013;378:15–24.
- [48] André D, Jebahi M, Charles JL, Iordanoff I, Nauport J. Using the discrete element method to simulate brittle fracture in the indentation of a silica glass with a blunt indenter. *Comput Methods Appl Mech Eng* 2013;265:136–47.
- [49] Guillebaud-Bonnafous C, Vasconcellos D, Touchard F, Chocinski-Arnault L. Experimental and numerical investigation of the interface between epoxy matrix and hemp yarn. *Compos Part A* 2012;43:2046–58.